Channel Measurements at 6.4 GHz for IEEE 802.11be WLAN

Nida Chaudhry
CWI, ECIT Institute
Queen's University Belfast
BT3 9DT, Belfast, UK
nchaudhry01@qub.ac.uk

Simon L. Cotton
CWI, ECIT Institute
Queen's University Belfast
BT3 9DT, Belfast, UK
simon.cotton@qub.ac.uk

Nidhi Simmons
CWI, ECIT Institute
Queen's University Belfast
BT3 9DT, Belfast, UK
nidhi.simmons@qub.ac.uk

Claudio R. C. M. Da Silva
Reality Labs
Meta Platforms
Redmond, WA, USA
claudiodasilva@meta.com

Okan Yurduseven
CWI, ECIT Institute
Queen's University Belfast
BT3 9DT, Belfast, UK
okan.yurduseven@qub.ac.uk

Paschalis C. Sofotasios
Center for Cyber-Physical Systems
Khalifa University
Abu Dhabi, UAE
p.sofotasios@ieee.org

Michail Matthaiou
CWI, ECIT Institute
Queen's University Belfast
BT3 9DT, Belfast, UK
m.matthaiou@qub.ac.uk

Trung Q. Duong
CWI, ECIT Institute
Queen's University Belfast
BT3 9DT, Belfast, UK
trung.q.duong@qub.ac.uk

Abstract—In this paper, we present the results of a set of channel measurements conducted within the 6 GHz band used in IEEE 802.11be based wireless local area networks (WLANs). A range of indoor and outdoor client to access point (AP) communication scenarios were considered for both line-of-sight (LOS) and non-LOS (NLOS) channel conditions. We have investigated the path loss, large-scale, and small-scale fading across 256 frequency points between 6.425 and 6.445 GHz. To model the large-scale fading we have utilized the lognormal and gamma distributions, while for the small-scale fading this was the Rayleigh, Rician, and Nakagami-m distributions. The information loss incurred when encoding the empirical distributions with the aforementioned theoretical ones was determined using the resistor-average distance (RAD). It was found that the gamma distribution provided a better fit to the large-scale fading, while the Rician and Nakagami-m distributions observed the lowest RAD values for the small-scale fading. To ascertain the temporal stability of the considered channels, the coherence time was inferred using an analysis of the autocorrelation. Our results indicate that the coherence time for the large-scale fading was typically longer than for small-scale fading.

Index Terms—Access point, autocorrelation, channel characterization, coherence time, large-scale fading, path loss, resistor-average distance (RAD), small-scale fading, sub-7 GHz, wireless local area network (WLAN).

I. INTRODUCTION

The ever-growing popularity of IEEE 802.11 based wireless local area network (WLAN) has seen it accounting for a significant portion of the mobile traffic carried globally [1]. Recently, Wi-Fi 6E [2] has seen considerable commercial success by extending the operational frequency range of Wi-Fi 6 networks. IEEE 802.11be [3], also known as Wi-Fi 7, is expected to enhance this even further, supporting emerging use cases such as the metaverse, augmented reality (AR), and ultra-high-definition (UHD) gaming by delivering significantly higher data rates [4].

In addition to the extremely high throughput (EHT), with data rates up to 46 Gbps, other key features of Wi-Fi 7 include
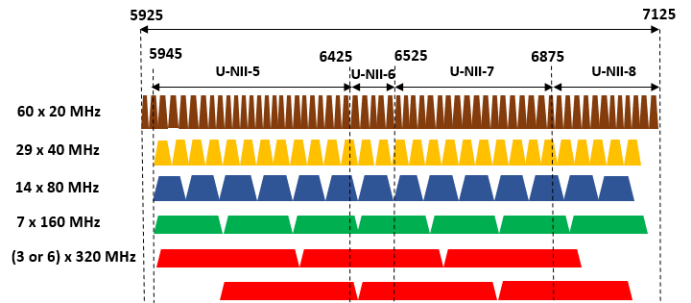
Fig. 1. Wi-Fi 7 Channelization

multi-link operation (MLO), multi-resource units (MRUs), 320 MHz wide channels, 4096-QAM modulation, triggered transmission opportunity (TXOP) sharing capability, preamble puncturing, hybrid automatic repeat request (HARQ), and up to 16 spatial streams to ensure high spectral efficiency [5]. The increased channel widths used by Wi-Fi 7 are closely linked to the availability of new spectrum between 5.9 and 7.1 GHz. Consequently, the demand for unlicensed spectrum has never been greater. The Federal Communications Commission (FCC) has recently proposed the unlicensed use of the 6 GHz band in the United States (US). This band is divided into four sub-bands, namely: U-NII-5 (5.925 – 6.425 GHz), U-NII-6 (6.425 – 6.525 GHz), U-NII-7 (6.525 – 6.875 GHz), and U-NII-8 (6.875 – 7.125 GHz) as shown in Fig. 1 [6].

To achieve improved performance and enable the optimal design of Wi-Fi 7 and future WLAN networks (including Wi-Fi 8), there is a need to rigorously study the channels within the 6 GHz band by conducting detailed channel measurements for different use cases and scenarios. To this end, the authors of [7] characterized multifrequency single-input–single-output (SISO) channels at 3 GHz, 5.5 GHz, and 6.5 GHz in large indoor office settings using a time-domain channel sounder. The study investigated the frequency dependence of the path loss, large-scale fading,

delay spread, and Rician K-factor. The authors observed a significant increase in the K-factor at higher frequencies, particularly for line-of-sight (LOS) scenarios. Conversely, the large-scale fading and delay spread exhibited a consistent behavior across all frequencies. Similarly, Zhou et al. [8] conducted wireless channel measurements for indoor corridor scenarios within the 2.4, 5, and 6 GHz bands using a time-domain channel sounder. The study presented an analysis of channel characteristics such as the average power delay profile (APDP), path loss, delay spread, and Rician K-factor as well as analyzing their frequency dependence.

In another study, Chrysikos et al. [9] performed channel measurements in multi-floored indoor and industrial environments at the 2.4 GHz for IEEE 802.11g. These channel measurements were used to characterize the path loss and large-scale fading. The results of this study provided a comparison of different path loss models, among which the Multi-Wall-Floor model performed better. The authors of [10] carried out channel measurements at 770 MHz, 2.401, and 5.540 GHz in indoor environments using a universal software radio peripheral (USRP). The study presented a characterization of IEEE 802.11ac and IEEE 802.11af based radio channels in terms of the wall attenuation factor (WAF), floor attenuation factor (FAF), and path loss. It was found that IEEE 802.11af benefited from stronger wall-penetration and smaller path loss compared to IEEE 802.11ac based radio channels. The majority of the existing Wi-Fi channel measurements have understandably been focused at sub-6 GHz frequency bands. However, few works have studied and characterized the path loss, large-scale and small-scale fading in the newly opened 6 GHz band using frequency domain channel sounding in both indoor and outdoor environments.

In this paper, we perform a statistical characterization and modeling of a 20 MHz region of spectrum defined in the IEEE 802.11be standard. To this end, we have conducted a series of frequency domain channel measurements over a range of indoor and outdoor scenarios, representative of the communication channel between a fixed access point (AP) and a hypothetical mobile client in both LOS and non-LOS (NLOS) settings. The measurements were used to characterize the radio channel in terms of the path loss, large-scale fading, and small-scale fading. Furthermore, an analysis of the autocorrelation was also performed to provide crucial insights into the channel coherence time ($\mathcal{T}_c$) of the large-scale and small-scale fading.

The rest of this paper is organized as follows. Section II describes the measurement set-up, environment, and procedure. In Section III, we present the models and techniques used to characterize the path loss, large-scale fading, small-scale fading, and channel coherence time. Our results and discussions are provided in Section IV along with a comparison against the different candidate fading models. Finally, some conclusions are drawn in Section V.
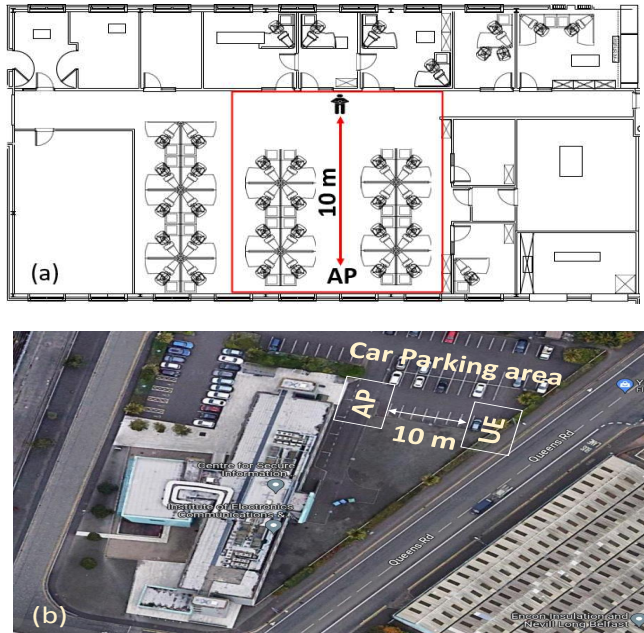
Fig. 2. Channel measurement environments showing (a) Floor plan of open office area (244.2 m^2) and (b) Satellite view of outdoor car parking area.

II. MEASUREMENT SET-UP, ENVIRONMENT, AND PROCEDURE

In this section, a series of channel measurements are described which were taken to understand part of the electromagnetic (EM) spectrum that will be used in future WLAN systems such as IEEE 802.11be based Wi-Fi 7 [3].

A. Measurement Set-up

The channel measurement set-up consisted of a compact two-port Keysight P5005B Streamline Vector Network Analyzer (VNA) and two omnidirectional 6.5 GHz ultra-wideband (UWB) AntennaWare BodyWave antennas with a uniform gain of +3dBi each. The transmit and receive antennas were connected to port 1 and port 2 of the VNA using two low-loss, phase-matched, flexible coaxial cables, with the transmit antenna enclosed in an acrylonitrile butadiene styrene (ABS) box (11 cm x 5.4 cm x 2 cm), emulating the client. The receive antenna was mounted on a telescopic pole at a height of 2.3 m mimicking an AP. In our measurements, we considered a 20 MHz region of the EM spectrum ranging from 6.425 to 6.445 GHz. To characterize this part of the spectrum, we split it up into 256 equispaced frequency points with a spacing of 78.125 kHz. These measurement settings were chosen to co-align with the center points of the subcarriers used by channel 97 of the IEEE 802.11be standard[1]. The VNA was connected to another laptop using an active fiber optical cable allowing remote control. The VNA was programmed to conduct continuous frequency sweeps across the 256 frequency points, and measure the complex forward path gain, S_{21}, with an IF bandwidth of

[1]This channel has 9 resource units (RUs) with 26 subcarriers in each, supporting 234 usable subcarriers along with 22 unusable subcarriers which include the guard band, direct conversion (DC), and null subcarriers.

10 kHz. A Hewlett Packard (HP) 85052D calibration kit was used to perform a pre-measurement calibration to mitigate the effects of cable losses. Subsequently, the average noise floor was determined before conducting the experiments and was found to be -105 dBm. It should be noted that 98% of the samples collected during the measurements were above the noise floor. A minimum of 750 repetitions were performed for each trial. The time taken for each sweep, including the time taken to write the measured data to the memory, was 53 ms.

B. Measurement Environment

The channel measurements were conducted in an indoor open office area of the three-story ECIT building at Queen's University Belfast, UK. Fig. 2(a) shows the plan view of the measurement environment relative to the rest of the open office area which was situated on the ground floor. The open office area featured metal-studded dry walls, a metal-tiled floor with polypropylene-fibre, rubber-backed carpet tiles, a metal ceiling with mineral fibre tiles, and louvered luminaries suspended at a height of 2.70 m above floor level. This environment also included multiple soft partitions and several fixtures such as metal cabinets, PCs, chairs, and desks made from medium-density fiberboard [11]. To ensure that the findings of this research are representative of the different environments Wi-Fi 7 networks will operate, we conducted another set of measurements in an outdoor parking area outside the three-story ECIT building at Queen's University Belfast, UK, as shown in the satellite view in Fig. 2(b).

C. Measurement Procedure

The measurements considered an adult female of height $1.59\,\mathrm{m}$ and mass 59 kg imitating four different use cases to represent the everyday client-to-AP usage. These use cases were: (1) imitating a voice call on the client i.e., a mobile phone/user equipment (UE) while holding the UE next to her left ear and approaching the AP; (2) making a voice call while holding the UE next to her right ear and receding away from the AP; (3) operating an app while holding the UE in front of her body and approaching the AP; and (4) operating an app while holding the UE in front of her body and walking away from the AP. Throughout all measurements, the person walked in a straight line and maintained an average walking velocity of $0.5\,\mathrm{m/s}$. The greatest separation distance between the person and the AP was $10\,\mathrm{m}$ and the shortest $1\,\mathrm{m}$. For the approaching measurements, the person started at the $10\,\mathrm{m}$ point and walked towards the AP, stopping at a distance of $1\,\mathrm{m}$ away. For the receding measurements they started at a distance of $1\,\mathrm{m}$ away from the AP and walked towards the $10\,\mathrm{m}$ point (see Fig. 2).

III. Data Analysis

Radio channels are often characterized in terms of path loss, large-scale, and small-scale fading. The path loss captures the attenuation of an RF signal between a transmitter (Tx) and a receiver (Rx) relative to the distance between them. It is commonly modeled using the log-distance path loss model. The log-distance path loss is usually measured in decibels, and modeled in terms of Tx-Rx separation distance (d). It can be expressed as

$$PL\,[\mathrm{dB}] = PL[d_0] + 10n\log_{10}\left(d/d_0\right), \quad d \geq d_0, \quad (1)$$

where d_0 is the reference distance, $PL\,[d_0]$ is the path loss at the reference distance d_0, and n is the path loss exponent.

Large-scale fading has traditionally been modeled using the lognormal distribution which describes the random shadowing effects that occur over a large number of measurement locations with the same Tx-Rx separation distance and different levels of environmental clutter. The cumulative distribution function (CDF) of the lognormal distribution may be written as [12]

$$F_P(p) = \frac{1}{2}\left[1 + \mathrm{erf}\left(\frac{\ln\left(p\right) - \mu}{\sqrt{2}\sigma}\right)\right], \quad (2)$$

where P is a random variable which models the fluctuation of the large-scale fading, μ is the location parameter, σ is the shape parameter, $\ln\left(.\right)$ is the natural logarithm, and $\mathrm{erf}(.)$ is the error function. Although the lognormal distribution has been extensively used to model shadowing, the gamma distribution is often used as an alternative owing to its tractability which renders it suitable for deriving other channel related statistics [13], [14]. The CDF of the gamma distribution is given by [15]

$$F_P(p) = \frac{\gamma(\alpha, p/\beta)}{\Gamma(\alpha)}, \quad (3)$$

where α represents the shape parameter, β is the scale parameter, $\Gamma(.)$ denotes the gamma function, and $\gamma(.)$ is the lower incomplete gamma function.

Previous channel studies have shown that small-scale fading can be modeled using the Rayleigh [16], Rician [17], and Nakagami-m distributions [18]. The Rayleigh distribution is commonly used to model the multipath fading signal when no LOS exists between the transmitter and receiver. Let R represent the envelope of the fading signal in a Rayleigh fading channel, where $2s^2$ is the mean signal power, then the CDF, $F_R(r)$, of R can be expressed as follows

$$F_R(r) = 1 - exp\left(-\frac{r^2}{2s^2}\right). \quad (4)$$

The Rician distribution plays a significant role in modeling a fading signal where a dominant path (such as LOS or a specular reflection) exists between a transmitter and receiver, in addition to scattered multipath. The CDF of the Rician distribution is given by

$$F_R(r) = 1 - Q_1\left(\frac{\delta}{s}, \frac{r}{s}\right), \quad (5)$$

where δ denotes the non-centrality parameter, s is the scaling parameter, and $Q_1(.)$ represents the Marcum Q-function. The Rician K-factor is a useful metric in the context of channel modeling, it is defined as the ratio of the power of

TABLE I
STATISTICS OF THE PARAMETER ESTIMATES FOR PATH LOSS, LARGE-SCALE FADING, AND SMALL-SCALE FADING ACROSS THE 256 SUBCARRIERS

Scenario	Statistics	Path loss		Large-scale fading						Small-scale fading								
				Lognormal			Gamma			Rayleigh		Rician				Nakagami-m		
		$\hat{n}$	$\hat{PL}[d_0]$	$\hat{\mu}$	$\hat{\sigma}$	RAD	$\hat{\alpha}$	$\hat{\beta}$	RAD	$\hat{s}$	RAD	$\hat{\delta}$	$\hat{s}$	$\hat{K}$	RAD	$\hat{m}$	$\hat{\Omega}$	RAD
Indoor App LOS	Min	1.46	49.34	-0.58	0.54	0.0191	2.02	0.17	**0.0101**	0.83	0.0142	0.03	0.46	0.00	**0.0039**	1.14	1.37	0.0056
	Max	1.84	52.22	-0.57	0.85	0.1320	3.76	0.36	**0.0431**	0.91	0.0571	0.97	0.91	2.24	**0.0350**	1.74	1.65	0.0266
	Median	1.60	51.06	-0.57	0.68	0.0584	2.54	0.27	**0.0155**	0.85	0.0356	0.95	0.51	1.72	**0.0101**	1.51	1.44	0.0105
	IQR	0.10	0.96	0.00	0.07	0.0451	0.28	0.04	**0.0095**	0.03	0.0154	0.04	0.08	0.60	**0.0094**	0.22	0.09	0.0061
Indoor App NLOS	Min	0.57	61.19	-0.59	0.45	0.0201	2.08	0.12	**0.0098**	0.87	0.0038	0.03	0.60	0.00	0.0035	0.84	1.53	**0.0041**
	Max	1.26	65.75	-0.57	0.78	0.1533	5.17	0.35	**0.0501**	1.00	0.0214	0.90	1.00	1.11	0.0214	1.32	2.01	**0.0168**
	Median	0.97	63.02	-0.58	0.56	0.0517	3.71	0.17	**0.0260**	0.91	0.0087	0.71	0.76	0.44	0.0080	1.15	1.64	**0.0078**
	IQR	0.08	0.75	0.00	0.07	0.0410	0.81	0.05	**0.0137**	0.03	0.0052	0.75	0.24	0.72	0.0037	0.15	0.12	**0.0032**
Indoor Call LOS	Min	1.18	56.15	-0.58	0.67	0.0304	1.64	0.26	**0.0061**	0.82	0.0170	0.03	0.46	0.00	0.0043	1.17	1.36	**0.0044**
	Max	1.56	58.76	-0.57	0.93	0.0972	2.63	0.48	**0.0266**	0.90	0.0702	0.97	0.90	2.21	0.0498	1.78	1.62	**0.0346**
	Median	1.38	57.53	-0.57	0.78	0.0491	2.03	0.36	**0.0137**	0.86	0.0309	0.93	0.55	1.38	0.0156	1.43	1.47	**0.0125**
	IQR	0.14	0.95	0.00	0.08	0.0207	0.28	0.06	**0.0057**	0.02	0.0157	0.05	0.07	0.51	0.0121	0.15	0.06	**0.0074**
Indoor Call NLOS	Min	1.10	57.50	-0.58	0.52	0.0227	2.18	0.15	**0.0107**	0.85	0.0045	0.03	0.51	0.00	0.0024	0.97	1.44	**0.0036**
	Max	1.50	60.21	-0.57	0.72	0.1792	4.13	0.33	**0.0495**	0.95	0.0344	0.96	0.95	1.73	0.0229	1.52	1.81	**0.0235**
	Median	1.26	58.88	-0.58	0.59	0.0854	3.29	0.20	**0.0198**	0.89	0.0135	0.84	0.67	0.80	0.0093	1.21	1.60	**0.0087**
	IQR	0.10	0.76	0.00	0.06	0.0803	0.62	0.05	**0.0130**	0.03	0.0123	0.21	0.15	0.63	0.0081	0.17	0.11	**0.0043**
Outdoor App LOS	Min	1.27	57.26	-0.58	0.50	0.1442	3.57	0.15	**0.1270**	0.71	1.4549	1.00	0.09	53.48	**0.0035**	27.07	1.01	0.0031
	Max	1.37	58.01	-0.57	0.56	0.2179	4.14	0.18	**0.1859**	0.71	1.6686	1.00	0.10	67.33	**0.0312**	34.17	1.02	0.0319
	Median	1.33	57.72	-0.58	0.53	0.1596	3.83	0.17	**0.1521**	0.71	1.5683	1.00	0.09	58.30	**0.0117**	29.57	1.02	0.0118
	IQR	0.05	0.32	0.00	0.03	0.0262	0.29	0.01	**0.0139**	0.00	0.0855	0.00	0.00	4.83	**0.0086**	2.54	0.00	0.0078
Outdoor App NLOS	Min	2.34	66.27	-0.59	0.61	0.0314	2.01	0.22	**0.0077**	0.82	0.0143	0.03	0.46	0.00	0.0046	1.13	1.35	**0.0054**
	Max	2.63	67.95	-0.57	0.82	0.1189	3.03	0.36	**0.0450**	0.91	0.0800	0.96	0.91	2.17	0.0594	1.81	1.66	**0.0415**
	Median	2.47	67.28	-0.58	0.69	0.0691	2.62	0.26	**0.0174**	0.86	0.0330	0.92	0.57	1.27	0.0190	1.39	1.49	**0.0157**
	IQR	0.09	0.41	0.00	0.05	0.0300	0.30	0.04	**0.0066**	0.02	0.0175	0.06	0.07	0.48	0.0118	0.14	0.07	**0.0078**
Outdoor Call LOS	Min	2.45	49.37	-0.58	0.81	0.2688	1.39	0.37	**0.0847**	0.71	0.9835	1.00	0.10	15.18	**0.0083**	8.18	1.02	0.0091
	Max	2.74	50.52	-0.57	1.09	0.3395	2.01	0.61	**0.1439**	0.73	1.5822	1.00	0.18	51.97	**0.2576**	25.83	1.06	0.3100
	Median	2.64	49.73	-0.58	0.93	0.2998	1.63	0.48	**0.1066**	0.72	1.3407	1.00	0.11	38.18	**0.0350**	19.18	1.03	0.0379
	IQR	0.12	0.52	0.00	0.14	0.0269	0.28	0.11	**0.0243**	0.00	0.1500	0.00	0.01	6.66	**0.0355**	3.38	0.00	0.0381
Outdoor Call NLOS	Min	1.26	68.64	-0.58	0.54	0.0197	1.39	0.16	**0.0094**	0.73	0.1842	0.98	0.18	3.70	**0.0048**	2.48	1.07	0.0066
	Max	2.20	74.10	-0.57	1.12	0.1826	4.08	0.61	**0.0845**	0.79	0.6786	1.00	0.36	14.75	**0.0845**	7.80	1.24	0.0860
	Median	1.76	71.89	-0.57	0.74	0.0568	2.16	0.33	**0.0433**	0.75	0.3831	1.00	0.25	8.19	**0.0224**	4.49	1.12	0.0274
	IQR	0.32	2.65	0.00	0.16	0.0420	0.78	0.15	**0.0219**	0.02	0.1985	0.00	0.06	3.83	**0.0194**	1.95	0.06	0.0197

the dominant component, δ^2, to the power of the scattered multipath component, $2s^2$, such that

$$K = \frac{\delta^2}{2s^2}. \quad (6)$$

The Nakagami-m distribution is typically used to model the multipath fading signal in NLOS channels. The CDF of the Nakagami-m distribution can be expressed as follows

$$F_R(r) = \frac{\gamma(m, mr^2/\Omega)}{\Gamma(m)}, \quad (7)$$

where m is the fading severity parameter and Ω is the mean power of the signal.

In order to quantify the information loss associated with using the aforementioned distributions to model the empirical distributions of the large-scale and small-scale fading, the resistor-average distance (RAD) [19] was calculated. The RAD is a symmetric version of Kullback-Leibler divergence (KLD) [20] and may be defined as

$$\text{RAD}(f_1, f_2) = \left(\frac{1}{\text{KLD}(f_1, f_2)} + \frac{1}{\text{KLD}(f_2, f_1)} \right)^{-1}, \quad (8)$$

where $\text{KLD}(f_1, f_2) = \int_{-\infty}^{\infty} f_1(x) \log_2 \left(\frac{f_1(x)}{f_2(x)} \right) dx$, with $f_1(x)$ and $f_2(x)$ denoting the empirical and theoretical PDFs, respectively.

The autocorrelation function (ACF) is a useful tool for studying the temporal behavior of a fading signal. It operates by assessing the similarity of a signal with itself over time [21]. The normalized autocorrelation, ρ_k, at a time lag k of the random process X can be written as

$$\rho_k = \frac{E[(X(t) - \mu_X)(X(t+k) - \mu_X)]}{\sqrt{E[(X(t) - \mu_X)^2]E[(X(t+k) - \mu_X)^2]}}, \quad (9)$$
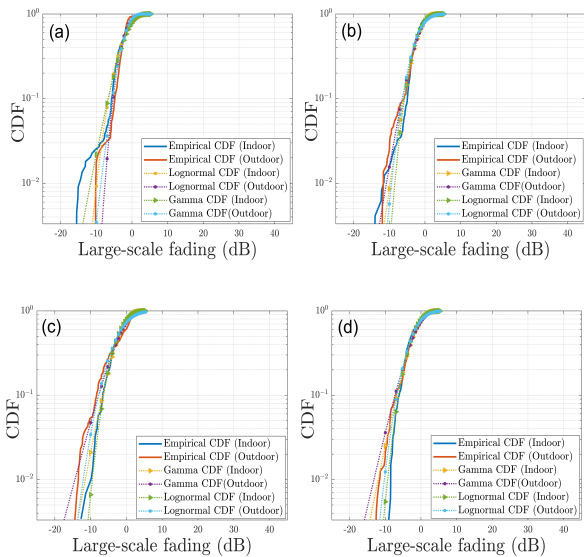
Fig. 3. CDFs of the lognormal and gamma distributions fitted to empirical data (subcarrier 1) for indoor and outdoor: (a) App LOS; (b) App NLOS; (c) Call LOS; and (d) Call NLOS measurement scenarios.

Fig. 4. CDFs of the Rayleigh, Rician, and Nakagami-m distributions fitted to empirical data (subcarrier 1) for indoor and outdoor: (a) App LOS; (b) App NLOS; (c) Call LOS; and (d) Call NLOS measurement scenarios.

where $E[.]$ is the expectation operator and μ_X is the mean of the random process. The channel coherence time, $\mathcal{T}_c$ is defined as the duration over which the autocorrelation function remains above a given threshold [22] and can be expressed as [23]

$$\mathcal{T}_c(\lambda) = k(\rho_k > \lambda) \cdot \mathcal{T}_s, \qquad (10)$$

where $\mathcal{T}_s$ represents the sampling time and $\lambda(0 \leq \lambda \leq 1)$ is the ACF threshold.

IV. RESULTS AND DISCUSSION

Over 3053 samples of the complex forward path gain, S_{21}, were considered for eight different measurement scenarios. The estimates of $PL[d_0]$ and n were calculated by initially transforming the magnitude of S_{21} into the received signal power in dBm. Subsequently, the sample acquisition time was mapped into distance using the average walking speed mentioned above. This process was repeated across all of the frequency points (subcarriers), followed by linear regression performed in MATLAB to obtain the parameter estimates for $PL[d_0]$ and n for each subcarrier. A summary of the results is presented in Table I, where the minimum, maximum, median, and interquartile range (IQR) of $\hat{PL}[d_0]$ and $\hat{n}$ across all subcarriers are presented. The results indicate that $\hat{n}$ was typically lower in the NLOS channels within indoor settings. This can be attributed to the waveguide effect caused by the surrounding wall and ceiling structures. Most notably, the impact of body shadowing was also evident in the results, where all of the estimates of $PL[d_0]$ were higher for the NLOS scenarios compared to their LOS equivalents.

The large-scale fading was then extracted by calculating the local mean over a distance of four wavelengths. Figs. 3(a)-(d) show some examples of the CDF of the lognormal and gamma distributions fitted to the empirical data (subcarrier 1) of the

indoor and outdoor app usage and call scenarios under LOS and NLOS channel conditions. The parameter estimates for both of the fading models were obtained using maximum-likelihood estimation (MLE) performed in MATLAB. Table I provides a summary of the parameter estimates across all of the subcarriers. It is noticeable that the medians of $\hat{\mu}$ for the lognormal distribution across both indoor and outdoor scenarios were similar. Moreover, $\hat{\sigma}$, which represents the spread of the lognormal distribution, was considerably higher in the outdoor scenarios with a median value of 0.93, particularly for the call LOS scenario. Similarly, $\hat{\beta}$ of the gamma distribution was also found to be higher in the outdoor scenarios with a median value of 0.48 for the call LOS scenario. To assess the goodness-of-fit of the lognormal and gamma fading models with the measured data, the RAD between the empirical and theoretical distributions was calculated. It is evident from Table I that the RAD for gamma distribution was lowest for all indoor and outdoor mobile scenarios, indicating that the gamma distribution actually performed better when modeling the large-scale fading in the scenarios considered in this study.

Consequently, both the path loss and large-scale fading were removed from the received signal power before transforming it into its linear amplitude to obtain the small-scale fading. The Rayleigh, Rician, and Nakagami-m distributions were used to model the small-scale fading and the parameter estimates were also obtained using MLE performed in MATLAB. As anticipated, the $\hat{K}$-factor was greater than unity in all indoor and outdoor LOS scenarios with medians of 1.72, 1.38, 58.30, and 38.18 for the indoor app LOS, indoor call LOS, outdoor app LOS, and outdoor call LOS scenarios, respectively, as shown in Table I. This suggests the presence of a dominant LOS component in these environments. The Rician distribution tended to provide a better fit to small-scale fading for the

TABLE II
SUMMARY OF STATISTICS OF THE COHERENCE TIME ACROSS ALL SUBCARRIERS

Scenario	Statistics	Large-scale fading				Small-scale fading			
		$\mathcal{T}_c$ (s)							
		$\lambda = 0.9$	$\lambda = 0.5$	$\lambda = 0.1$	$\lambda = 0$	$\lambda = 0.9$	$\lambda = 0.5$	$\lambda = 0.1$	$\lambda = 0$
Indoor App LOS	Min	0.106	0.266	0.478	0.637	0.053	0.053	0.053	0.106
	Max	0.106	0.372	0.85	2.497	0.053	0.053	0.106	0.106
	Median	0.106	0.319	0.584	0.903	-	0.053	0.106	0.106
	IQR	0.000	0.053	0.159	1.487	0.000	0.000	0.053	0.000
Indoor App NLOS	Min	0.053	0.212	0.372	0.372	0.053	0.053	0.053	0.053
	Max	0.106	0.319	0.691	1.169	0.053	0.053	0.053	0.106
	Median	0.106	0.266	0.478	0.531	-	-	0.053	0.106
	IQR	0.000	0.053	0.106	0.212	0.000	0.000	0.000	0.000
Indoor Call LOS	Min	0.053	0.159	0.372	1.275	0.053	0.053	0.053	0.053
	Max	0.106	0.266	2.019	3.772	0.053	0.053	0.053	0.053
	Median	0.053	0.212	0.956	2.125	-	-	-	0.053
	IQR	0.000	0.000	0.319	0.903	0.000	0.000	0.000	0.000
Indoor Call NLOS	Min	0.053	0.159	0.319	0.319	0.053	0.053	0.053	0.053
	Max	0.106	0.266	1.328	2.762	0.053	0.053	0.053	0.106
	Median	0.053	0.212	0.372	0.744	-	-	-	0.053
	IQR	0.053	0.053	0.319	0.637	0.000	0.000	0.000	0.053
Outdoor App LOS	Min	0.159	0.425	0.956	1.806	0.053	0.053	0.106	0.106
	Max	0.159	0.478	1.062	2.072	0.053	0.053	0.106	0.106
	Median	0.159	0.478	0.956	1.912	-	0.053	0.106	0.106
	IQR	0.000	0.000	0.053	0.106	0.000	0.000	0.000	0.000
Outdoor App NLOS	Min	0.053	0.266	0.425	0.478	0.053	0.053	0.053	0.053
	Max	0.106	0.372	0.691	1.912	0.053	0.053	0.053	0.053
	Median	0.106	0.319	0.531	0.637	-	-	-	0.053
	IQR	0.000	0.053	0.106	0.106	0.000	0.000	0.000	0.000
Outdoor Call LOS	Min	0.159	1.169	2.815	3.347	0.053	0.053	0.053	0.053
	Max	0.212	1.541	3.240	3.665	0.053	0.053	0.106	0.106
	Median	0.212	1.328	3.081	3.453	-	-	0.053	0.106
	IQR	0.053	0.212	0.212	0.159	0.000	0.000	0.000	0.000
Outdoor Call NLOS	Min	0.106	0.372	0.903	1.594	0.053	0.053	0.053	0.053
	Max	**0.266**	**1.009**	**3.187**	**4.303**	0.053	0.053	0.106	0.106
	Median	0.159	0.531	1.753	2.470	-	-	0.053	0.106
	IQR	0.053	0.319	1.195	1.169	0.000	0.000	0.053	0.000

majority of the LOS scenarios. Whereas, the Nakagami-m distribution proved to be a more suitable fit to small-scale fading for most of the NLOS scenarios. Here the $\hat{m}$ parameter was found to be greater than 1, which suggests clustering in the channel. As examples of the small-scale fading, Figs. 4(a)-(d) show the CDF of the Rayleigh, Rician, and Nakagami-m distributions fitted to the empirical data (subcarrier 1) for all of the indoor and outdoor app usage and call scenarios in LOS and NLOS channel conditions.

To investigate the temporal stability of the channel, at both the large-scale and small-scale levels, across the different frequency points, we analyzed the autocorrelation function using the `autocorr(.)` function available in the econometrics toolbox of MATLAB. From this, we obtained the coherence time. For our analysis, we set the ACF thresholds (λ) to be to 0.9, 0.5, 0.1, and 0, where 0 was selected specifically to determine the first instance where the fading signal decorrelates completely. Table II presents a summary of the coherence time for the large-scale and small-scale fading across all subcarriers for the given thresholds. It can be seen in Table II that some entries for the median $\mathcal{T}_c$ are marked with dashes (-) at certain ACF threshold levels for the small-scale fading rather than specific values of the $\mathcal{T}_c$. The reason

for this is that ACF of the small-scale fading crosses the given threshold level within the sample period. It is shown in Table II that the large-scale fading frequently exhibits longer coherence times, in comparison to small-scale fading.

This trend is highlighted in the indoor NLOS scenarios, especially at the 0.9 and 0.5 thresholds as shown in Table II. For instance, the maximum value of the $\mathcal{T}_c$ for the large-scale fading of the outdoor call NLOS scenario is 0.266 s, 1.009 s, and 3.187 s for the thresholds of 0.9, 0.5, and 0.1, respectively. The large-scale fading in this channel completely decorrelates at 4.303 s. In contrast, the small-scale fading manifested consistently short $\mathcal{T}_c$ across all scenarios. In many instances, the median $\mathcal{T}_c$ values suggested that the small-scale fading had completely decorrelated within 100 ms (and in many cases sooner). This behavior aligns with the rapid variations associated with the small-scale fading due to the multipath. The results show the contrasting temporal behavior of the fading at the large- and small-scale, providing valuable insights for the design and optimization of future Wi-Fi systems. Figs. 5(a)-(d) show some example ACF plots for the large-scale and small-scale fading (subcarrier 1) of the indoor and outdoor app usage and call scenarios under LOS and NLOS channel conditions, respectively.
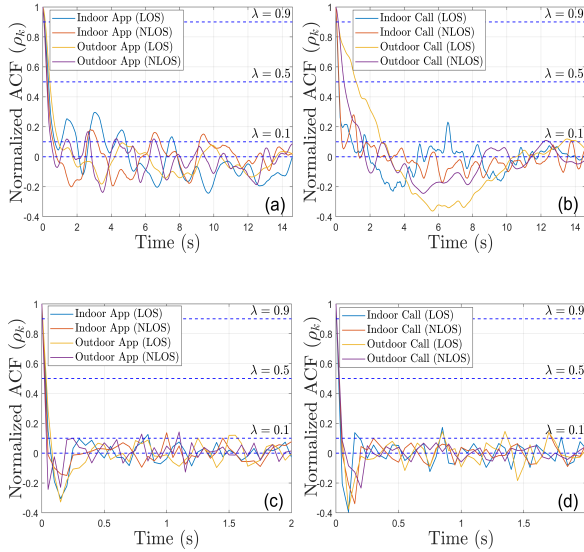
Fig. 5. ACF plots for the large-scale fading of the indoor and outdoor: (a) App usage and; (b) Call measurement scenarios; and for the small-scale fading of the indoor and outdoor: (c) App usage and; (d) Call measurement scenarios in LOS and NLOS channel conditions.

V. CONCLUSION

In this paper, the characteristics of a 20 MHz section of EM spectrum between 6.425 and 6.445 GHz, which will be used by IEEE 802.11be based WLANs, has been studied. Parameter estimates for the path loss, large-scale, and small-scale fading under eight separate indoor and outdoor LOS and NLOS scenarios have been obtained using MLE. Results obtained using the RAD have indicated that the gamma distribution provided a better fit to the large-scale fading than the more popular lognormal distribution. Whereas, the Rician and Nakagami-m fading models were favored for the small-scale fading across most of the subcarriers for a majority of LOS and NLOS mobile scenarios, respectively. Lastly, the stark differences between the temporal stability of the considered channels at the large and small scales have been highlighted. Notably the estimated coherence time of the large-scale fading was typically greater than that of the small-scale fading, particularly at the lower threshold levels.

ACKNOWLEDGMENT

REFERENCES

[1] J. Lee, D. An, and I. Yeom, "Analaysis of bit error in wireless LAN," in *2015 International Conference on Information Networking (ICOIN)*, pp. 529–530, IEEE, 2015.

[2] H. Brunner *et al.*, "Understanding and mitigating the impact of Wi-Fi 6E interference on ultra-wideband communications and ranging," in *2022 21st ACM/IEEE International Conference on Information Processing in Sensor Networks (IPSN)*, pp. 92–104, IEEE, 2022.

[3] C. Chen *et al.*, "Overview and performance evaluation of Wi-Fi 7," *IEEE Communications Standards Magazine*, vol. 6, no. 2, pp. 12–18, 2022.

[4] C. Deng *et al.*, "IEEE 802.11be Wi-Fi 7: New challenges and opportunities," *IEEE Communications Surveys & Tutorials*, vol. 22, no. 4, pp. 2136–2166, 2020.

[5] E. Reshef and C. Cordeiro, "Future directions for Wi-Fi 8 and beyond," *IEEE Communications Magazine*, vol. 60, no. 10, pp. 50–55, 2022.

[6] G. Naik, J. M. Park, J. Ashdown, and W. Lehr, "Next generation Wi-Fi and 5G NR-U in the 6 GHz bands: Opportunities and challenges," *IEEE Access*, vol. 8, pp. 153027–153056, 2020.

[7] L. Zhang *et al.*, "Multifrequency wireless channel measurements and characterization in large indoor office environments," *IEEE Transactions on Antennas and Propagation*, vol. 71, pp. 5221–5234, June 2023.

[8] Z. Zhou *et al.*, "Multi-frequency wireless channel measurements and characteristics analysis in indoor corridor scenarios," in *2021 IEEE 94th Vehicular Technology Conference (VTC2021-Fall)*, pp. 1–5, IEEE, 2021.

[9] T. Chrysikos *et al.*, "Channel measurement and characterization for a complex industrial and office topology at 2.4 GHz," in *11th International Conference on Software, Knowledge, Information Management and Applications (SKIMA)*, pp. 1–8, IEEE, 2017.

[10] G. Hwang *et al.*, "Measurement and comparison of Wi-Fi and super Wi-Fi indoor propagation characteristics in a multi-floored building," *Journal of Communications and Networks*, vol. 18, no. 3, pp. 476–483, 2016.

[11] S. L. Cotton and W. G. Scanlon, "A statistical analysis of indoor multipath fading for a narrowband wireless body area network," in *2006 IEEE 17th International Symposium on Personal, Indoor and Mobile Radio Communications*, pp. 1–5, IEEE, 2006.

[12] C. Walck *et al.*, *Hand-book on statistical distributions for experimentalists*. Stockholms universitet, 1996.

[13] G. L. Stüber, *Principles of mobile communication*, vol. 2. Springer, 2001.

[14] A. Abdi and M. Kaveh, "On the utility of gamma pdf in modeling shadow fading (slow fading)," in *1999 IEEE 49th Vehicular Technology Conference (Cat. No. 99CH36363)*, vol. 3, pp. 2308–2312, IEEE, 1999.

[15] S. K. Yoo *et al.*, "Measurements of the 60 GHz UE to eNB channel for small cell deployments," *IEEE Wireless Communications Letters*, vol. 6, no. 2, pp. 178–181, 2017.

[16] H. Janes and P. Wells, "Some tropospheric scatter propagation measurements near the radio horizon," *Proceedings of the IRE*, vol. 43, no. 10, pp. 1336–1340, 1955.

[17] S. K. Yoo *et al.*, "Channel characteristics of dynamic off-body communications at 60 GHz under line-of-sight (LOS) and non-LOS conditions," *IEEE Antennas and Wireless Propagation Letters*, vol. 16, pp. 1553–1556, 2017.

[18] M. Nakagami, "The m-distribution—A general formula of intensity distribution of rapid fading," in *Statistical methods in radio wave propagation*, pp. 3–36, Elsevier, 1960.

[19] D. Johnson and S. Sinanovic, "Symmetrizing the Kullback-Leibler distance," *IEEE Transactions on Information Theory*, 2001.

[20] S. Kullback, *Information theory and statistics*. Courier Corporation, 1997.

[21] S. L. Cotton and W. G. Scanlon, "Channel characterization for single- and multiple-antenna wearable systems used for indoor body-to-body communications," *IEEE Transactions on Antennas and Propagation*, vol. 57, no. 4, pp. 980–990, 2009.

[22] T. S. Rappaport, "Wireless communications–principles and practice," *Microwave Journal*, vol. 45, no. 12, pp. 128–129, 2002.

[23] L. Zhang *et al.*, "An RSS-based classification of user equipment usage in indoor millimeter wave wireless networks using machine learning," *IEEE Access*, vol. 8, pp. 14928–14943, 2020.